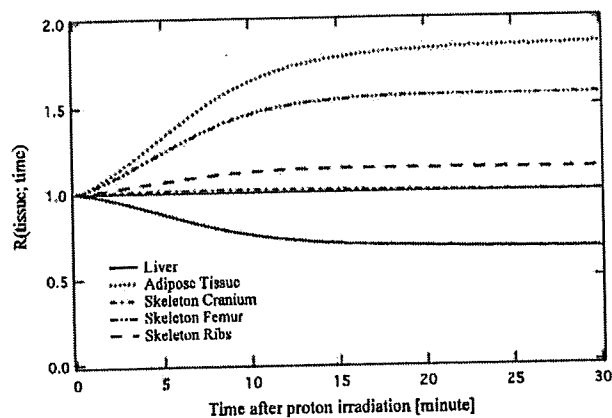**Fig. 5** Dose distribution calculated with the proton treatment planning system and activity measured with the PET-CT apparatus on CT image after proton treatment of liver tumor following TACE. The iso-dose line of 100% is red, 80% yellow green, 50% light blue, and 20% purple. The activity line of 7 kBq/cc is red, 5 kBq/cc green, and 3 kBq/cc bule. Proton beam irradiation was performed with an SOBP of 80 mm, gantry angle of 180 degrees and dose of 3.8 GyE. The dose distributions on each CT image in axial and coronal planes are shown in figures (a) and (b), and the activity are shown in figures (c) and (d)
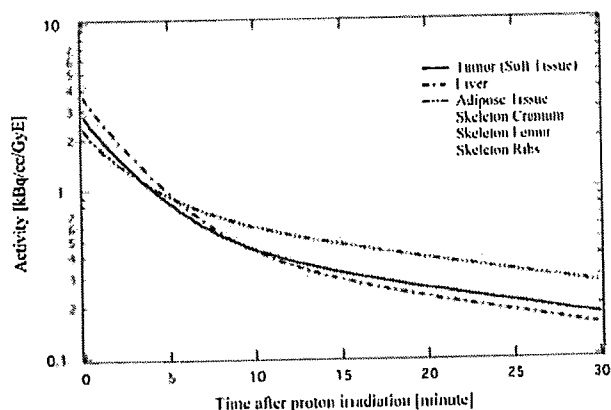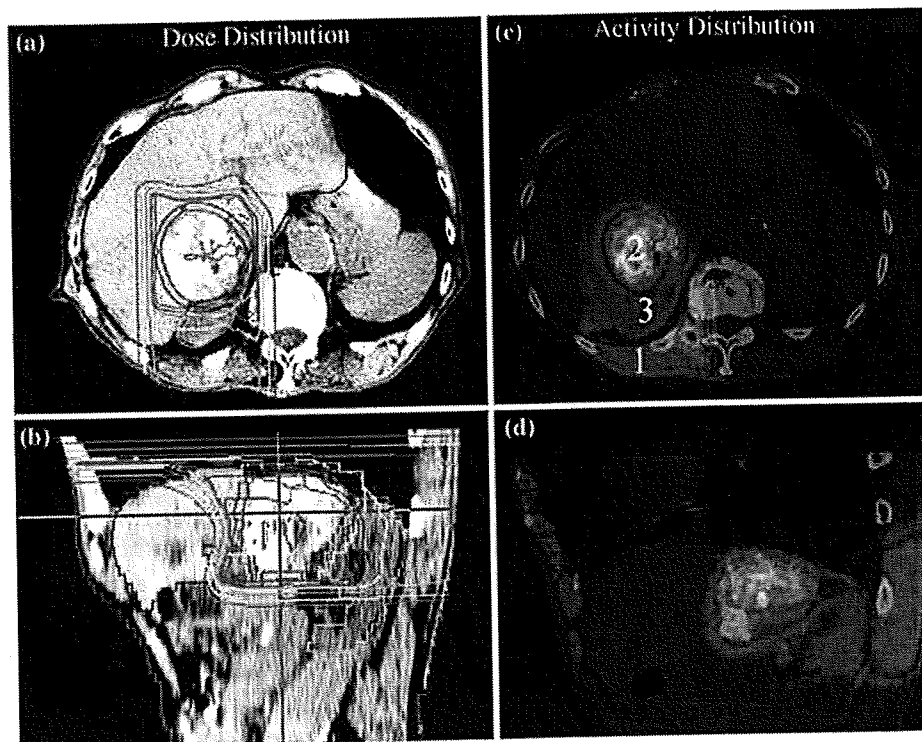
Fig. 6 Calculated activity $N_{\beta+}$ to the interval between the stopping beam and starting measurement of the activity in various tissues

Fig. 7 Ratio R of the calculated activity normalized to one at $T_0 = 0$ in various tissues

Table 1 Data of human body composition and proton energy used for the calculation of the time dependent activity in various tissues

Body tissue	n_{tissue} $(X)(10^{22}/cm^3)$					Proton energy (MeV)
	H	C	N	O	Other (Ca)	
Tumor (soft tissue)	6.6	1.3	0.1	2.4	0.0	60.4
Liver	6.6	0.7	0.1	2.9	0.0	70.6
Adipose tissue	6.6	2.5	0.1	1.3	0.0	114.3
Skeleton cranium	5.9	2.1	0.3	3.2	0.3	89.1
Skeleton femur	6.4	2.6	0.2	2.1	0.1	141.6
Skeleton ribs	6.3	2.1	0.3	2.7	0.2	109.6

"Calculation: C" in Table 3 is the calculated activity in the simulation of the 5 min measurement with a PET apparatus immediately after the proton irradiation. As a result, it was estimated that the activity was about 10 kBq/cc per 2.5-GyE dose immediately after the proton irradiation.

The biological washout effect will greatly affect the accuracy of the measured activity. The coefficient of the effect has been estimated to be the 50–65% of total activity [23, 24]. However, the radioactive ion beam was irradiated to a living tissue in the study. A flow-out of the positron-emitting nuclei implanted by the radioactive ion

Table 2 Proton energy, reaction cross section, half life used for the calculation of the activity in human body

Treatment site	Interest point	Proton energy (MeV)	Irradiation dose (GyE)	Cross section (mb)															
				Target nuclei PositronEmitting nuclei Half life (min)															
				^{12}C ^{11}C 20.39	^{12}C ^{10}C 0.321	^{14}N ^{13}N 9.965	^{14}N ^{11}C 20.39	^{14}N ^{10}C 0.321	^{16}O ^{15}O 2.037	^{16}O ^{14}O 1.177	^{16}O ^{13}N 9.965	^{16}O ^{11}C 20.39	^{16}O ^{10}C 0.321	^{40}Ca ^{38}K 7.636	^{40}Ca ^{30}P 2.498	^{40}Ca ^{15}O 2.037	^{40}Ca ^{13}N 9.965	^{40}Ca ^{11}C 20.39
Sacrum	1	73.1	2.5	81.3	4.4	16.1	52.4	6.5	69.8	1.7	6.6	18.2	1.8	14.1	9.2	2.2	2.2	2.2
	2	48.4	2.5	95.6	5.2	24.1	65.3	8.0	71.0	1.7	6.8	14.9	1.9	14.1	9.2	2.2	2.2	2.2
	3	62.1	2.5	88.9	4.8	6.6	18.6	1.9	70.9	1.7	6.6	18.6	1.9	14.1	9.2	2.2	2.2	2.2
Prostate	1	173.0	1.4	50.3	2.7	8.1	13.7	1.7	35.1	0.8	6.6	10.4	0.9	14.1	9.2	2.2	2.2	2.2
	2	137.7	1.4	54.4	2.9	14.9	11.6	1.4	44.3	1.1	6.6	12.1	1.2	14.1	9.2	2.2	2.2	2.2
	3	63.3	2.0	88.1	4.8	19.0	58.6	7.2	70.8	1.7	6.6	18.6	1.9	14.1	9.2	2.2	2.2	2.2
Head and neck	1	103.3	2.7	64.2	3.5	12.3	33.3	4.1	59.4	1.4	6.6	15.2	1.6	14.1	9.2	2.2	2.2	2.2
	2	70.4	3.7	83.2	4.5	16.9	54.1	6.7	70.2	1.7	6.6	18.4	1.9	14.1	9.2	2.2	2.2	2.2
	3	115.9	1.7	59.6	3.2	13.2	25.4	3.1	53.4	1.3	6.6	13.8	1.4	14.1	9.2	2.2	2.2	2.2
Liver	1	121.1	3.2	58.1	3.1	13.6	22.1	2.7	51.1	1.2	6.6	13.4	1.3	14.1	9.2	2.2	2.2	2.2
	2	75.9	3.8	79.4	4.3	15.2	50.6	6.2	69.3	1.6	6.6	18.0	1.8	14.1	9.2	2.2	2.2	2.2
	3	100.8	3.8	65.3	3.5	12.1	34.9	4.3	60.6	1.4	6.6	15.5	1.6	14.1	9.2	2.2	2.2	2.2
Liver	1	131.9	3.1	55.5	3.0	14.5	15.3	1.9	46.5	1.1	6.6	12.5	1.2	14.1	9.2	2.2	2.2	2.2
	2	71.8	3.8	82.2	4.4	16.5	53.2	6.6	70.0	1.7	6.6	18.3	1.8	14.1	9.2	2.2	2.2	2.2
	3	110.0	3.4	61.6	3.3	12.8	29.1	3.6	56.2	1.3	6.6	14.5	1.5	14.1	9.2	2.2	2.2	2.2

beam is the washout effect. On the other hand, in our study, the positron-emitting nuclei are generated from the nuclei in a tissue constituting a human body. Therefore, physiology, the effect has a different possibility. Perhaps, it is guessed that the effect may be not too large at our study.

The measured and calculated activities summarized in Table 3 will have the large error bar of a few 10%, and be scarcely correspondent within the large error bar in the soft tissue and the bone tissue except a skeleton femur. The measured activities in the subcutaneous adipose tissue, the skeleton femur, and the liver tumor after a TACE procedure are about two to three times higher than the calculated activities. Anyway the reason of large disagreement is not clear.

3.3 Comparison between proton dose distribution and activity distribution

The activity distribution visually corresponded to the proton dose distribution in Figs. 1, 2, 3, 4 and 5. Figure 8 shows the dose and activity distributions with a spike shape on the sagittal CT image in the head and neck. The position of the dose and activity distributions of the spike shape was consistent. However, it is difficult to show the correspondence quantitatively. We have executed the quantitative evaluation concerning the correspondence of the proton dose distribution and the activity distribution by our previous research [11, 13]. As the results, the activity range was about 7 mm shorter in a water equivalent length than the proton range expected from the energy threshold for the

Table 3 Proton irradiation dose, irradiation time, time of activity measurement, and level of activity measured and calculated

Treatment site	Irradiation dose (GyE/fx.)	Irradiation time (s)	Interval between stopping beam and starting measurment (s)	Point	Irradiation dose (GyE)	Activity (kBq/cc) Measurement:A	Calculation:B	A/B	Activity (kBq/cc) Calculation:C
Sacrum	2.5	55	430	1	2.5	3.8(± 0.5)	1.7(± 0.4)	2.2(± 0.6)	5.5(± 1.2)
				2	2.5	1.8(± 0.2)	2.1(± 0.4)	0.9(± 0.5)	8.5(± 1.8)
				3	2.5	2.5(± 0.3)	2.5(± 0.5)	1.0(± 0.6)	10.2(± 2.1)
Prostate	2.0	41	450	1	1.4	4.6(± 0.6)	1.1(± 0.2)	4.2(± 0.7)	3.3(± 0.7)
				2	1.4	4.2(± 0.6)	1.8(± 0.4)	2.3(± 0.7)	6.7(± 1.4)
				3	2.0	1.2(± 0.2)	1.3(± 0.3)	0.9(± 0.3)	6.1(± 1.3)
Head and neck	4.0	45	436	1	2.7	4.4(± 0.6)	1.7(± 0.4)	2.6(± 0.7)	3.0(± 0.6)
				2	3.7	3.0(± 0.4)	4.1(± 0.9)	0.7(± 0.9)	25.1(± 5.2)
				3	1.7	1.1(± 0.1)	1.4(± 0.3)	0.8(± 0.3)	13.1(± 2.7)
Liver	3.8	108	390	1	3.2	7.5(± 1.0)	2.4(± 0.5)	3.1(± 1.1)	6.5(± 1.4)
				2	3.8	2.3(± 0.3)	2.6(± 0.5)	0.9(± 0.6)	12.8(± 2.7)
				3	3.8	2.6(± 0.3)	2.8(± 0.6)	0.9(± 0.7)	13.6(± 2.8)
Liver	3.8	158	505	1	3.1	3.6(± 0.5)	2.0(± 0.4)	1.8(± 0.6)	5.8(± 1.2)
				2	3.8	6.9(± 0.9)	1.8(± 0.4)	3.8(± 1.0)	11.0(± 2.3)
				3	3.4	2.3(± 0.3)	1.8(± 0.5)	1.2(± 0.5)	11.1(± 2.3)

Fig. 8 Dose distribution and activity distribution on CT image after proton treatment of tumor in the head and neck. The *arrow* indicates the dose point of the spike shape
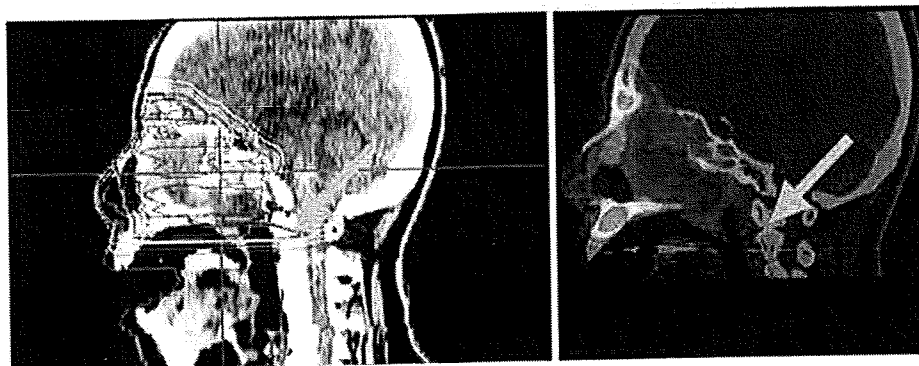
nuclear fragmentation reaction in a mono-energetic proton beam. Moreover, it was confirmed that the lateral activity distribution corresponds to the real beam size with an accuracy within 1 mm. In the therapeutic SOBP proton beam, the difference of the range between proton beam and the activity is larger than the case of a mono-energetic proton beam. Moreover, the therapeutic SOBP beam deteriorates the correspondence between the lateral dose and the activity distributions.

There is no simple relation between the stopping power of proton beam that determines the proton dose distribution and the cross section of the nuclear fragmentation reaction expressed as Eq. 1. Therefore, the activity distribution has no sharp peak like the Bragg peak in the proton dose distribution. For a proton therapy, it is very large impact to monitor the therapeutic proton dose distribution by use of the activity distribution in a patient. Therefore, it is necessary to innovatively research the physical reaction mechanism of the nuclear fragmentation reaction.

In the position of the proton-irradiated volume in the patient, the accuracy at the lateral dose and activity distributions will be about half cm, and the accuracy at the distal distributions cm order by the effects of the energy threshold for the nuclear fragmentation reaction and the SOBP width in the target organ without the respiratory motion (head and neck, etc). On the other hand, the accuracy at the lateral dose and activity distributions will be a few cm on the direction of the organ motion especially in the target organ with the respiratory motion (liver, etc) for the PET measurement without synchronization. In a proton treatment planning at our facility, planning target volume (PTV) has the margin of 3–10 mm in clinical target volume (CTV) by each treatment site. It will be visually confirmed whether gross tumor volume (GTV) is inside the proton-irradiated field.

4 Conclusion

In proton therapy, the proton-irradiated volume in the patient body was visually confirmed by measurement of the activity of the positron-emitting nuclei generated by the nuclear fragmentation reaction by use of the PET-CT apparatus. Moreover, verifications of the distribution and intensity of activity were performed for each body tissue composition. As yet, quantitative evaluations of the absolute activities remain.

To date, the acquisitions of PET and CT images were executed separately by use of each apparatus [7, 9]. There was a limit on the precision of image fusion. Therefore, determining whether the activity in the ribs or subcutaneous adipose tissue was high was previously very difficult after proton treatment of liver and lung cancers [7]. In this

study, the confirmation of high activity in subcutaneous adipose tissue demonstrated the advantage of using PET-CT apparatus. The high activity in liver tumors, TACE may be used for dose-reference marker of the proton beam irradiation.

In the result, it was suggested that the events of the activity detected by use of the BOLPs provided enough data for reconstruction of the PET image. The clinical use of this information about the positron-emitting nuclei generated will be important for promoting proton treatment with higher accuracy in the future. For that reason, it will be necessary to much-improve the accuracy of the measured and calculated activity for the innovative proton therapy in which the irradiation position is especially controlled within a few mm in the treatment site with high accuracy of the patient positioning such as head and neck.

References

1. Chu WT, Ludewigt BA, Renner TR. Instrumentation for treatment of cancer using proton and light-ion beams. Rev Sci Instrum. 1993;64(8):2055–122.
2. Bennett GW, Goldberg A, Levine G, Guthy J, Balsamo J. Beam localization via 15O activation in proton radiation therapy. Nucl Instr Meth. 1975;125:333–8.
3. Bennett GW, Archambeau JO, Archambeau BE, Meltzer JI, Wingate CL. Visualization and transport of positron emission from proton activation in vivo. Science. 1978;200:1151–3.
4. Oelfke U, Lam G, Atkins M. Proton dose monitering with PET: quantiative studies in Lucite. Phys Med Biol. 1996;41:177–96.
5. Litzenberg DW, Roberts DA, Lee MY, Pham K, Vander Molen AM, Ronningen R, et al. On-line monitoring of radiotherapy beams: experimental results with proton beams. Med Phys. 1999;26(6):992–1006.
6. Parodi K, Enghardt W. Potential application of PET in quality assuarnce of proton therapy. Phys Med Biol. 2000;45:N151–6.
7. Nishio T, Ogino T, Shimbo M, Katsuta S, Kawasaki S, Murakami T, et al. Distributions of β^+ decayed nucleus produced from the target fragment reaction in (CH$_2$) n and patient liver targets by using a proton beam for therapy. Abstracts of the XXXIV PTCOG MEETING in Boston; 2001. pp. 15–6.
8. Parodi K, Enghardt W, Haberer T. In-beam PET measurements of β^+ radioactivity induced by proton beams. Phys Med Biol. 2002;47:21–36.
9. Hishikawa Y, Kagawa K, Murakami M, Sasaki H, Akagi T, Abe M. Usefulness of positron-emission tomographic images after proton therapy. Int J Rad Oncol Biol Phys. 2002;53:1388–91.
10. Enghardt W, Crespo P, Fiedler F, Hinz R, Parodi K, Pawelke J, et al. Dose quantification from in-beam positron emission tomography. Radiother Oncol. 2004;73(Suppl. 2):S96–8.
11. Nishio T, Sato T, Kitamura H, Murakami K, Ogino T. Distributions of β^+ decayed nuclei generated in the CH$_2$ and H$_2$O

targets by the target nuclear fragment reaction using therapeutic MONO and SOBP proton beam. Med Phys. 2005;32(4):1070–82.

12. Parodi K, Ponisch F, Enghardt W. Experimental study on the feasibility of in-beam PET for accurate monitoring of proton therapy. IEEE Trans Nucl Sci. 2005;52:778–86.

13. Nishio T, Ogino T, Nomura K, Uchida H. Dose-volume delivery guided proton therapy using beam ON-LINE PET system. Med Phys. 2006;33(11):4190–7.

14. Photon, Electron, Proton and Neutron Interaction Data for Body Tissues (ICRU Report 46). pp. 11–3.

15. Iljinov AS, Semenov VG, Semenova MP, Schopper H. Interactions of protons with nuclei (supplement to I/13a, b, c), (Landolt-Bornstein New Series. 1994).

16. Goldharber AS. Statistical models of fragmentation processes. Phys Lett. 1974;53B:306–8.

17. Winger A, Sherrill BM. Morrissey. INTENSITY: acomputer program for the estimation of secondary beam intensities from a projectile fragment separator. Nucl Instrum Methods. 1992;B70:380–92.

18. Nishio T. Proton therapy facility at National Cancer Center, Kashiwa, Japan. J At Energy Soc. 1999;41(11):1134–8.

19. Tachikawa T, Sato T, Ogino T, Nishio T. Proton treatment devices at National Cancer Center (Kashiwa). Radiat Indust. 1999;84:48–53.

20. Nishio T, Kataoka S, Tachibana M, Matsumura K, Uzawa N, Saito H, et al. Development of a simple control system for unifom proton dose distribution in a dual-ring double scattering system. Phys Med Biol. 2006;51:1249–60.

21. Nishio T, Ogino T, Sakudo M, Tanizaki N, Yamada M, Nishida G, et al. Present proton treatment planning system at National Cancer Center Hospital East. Jpn J Med Phys Proc. 2000;20(Suppl. 4):174–7.

22. Boellaard R, Lingen AV, Lammertsma AA. Experimental and clinical evaluation of iterative reconstruction (OSEM) in dynamic PET: quantitative characteristics and effects on kinetic modeling. J Nucl Med. 2001;42:808–17.

23. Tomitani T, Pawelke J, Kanazawa M, Yoshikawa K, Yoshida K, Sato M, et al. Washout studies of ^{11}C in rabbit thigh muscle implanted by secondary beams of HIMAC. Phys Med Biol. 2003;48:875–89.

24. Mizuno H, Tomitani T, Kanazawa M, Kitagawa A, Pawelke J, Iseki Y, et al. Washout measurement of radioisotope implanted by radioactive beams in the rabbit. Phys Med Biol. 2003;48:2269–81.

ORIGINAL ARTICLE

Experimental verification of the utility of positron emitter nuclei generated by photonuclear reactions for X-ray beam monitoring in a phantom

Teiji Nishio · Taku Inaniwa · Kazumasa Inoue
Aya Miyatake · Keiichi Nakagawa · Kiyoshi Yoda
Takashi Ogino

Abstract

Purpose. The utility of positron emitter nuclei generated by photonuclear reactions was verified for X-ray beam monitoring in a phantom.

Materials and methods. Positron emission tomography-computed tomography (PET-CT) images of a gelatinous water phantom (H_2O target) and a polyethylene phantom (CH_2 target) were acquired 5 min after delivering a dose of 17 Gy with an X-ray beam energy of 21 MV. Reconstructed PET images and the calculated half-life showed that the positron emitters of ^{15}O (half-life 122.2 s) in the

T. Nishio (✉) · T. Ogino
Particle Therapy Division, Research Center for Innovative Oncology, National Cancer Center, 6-5-1 Kashiwano-ha, Kashiwa 277-8577, Japan
Tel. +81-4-7133-1111; Fax +81-4-7134-7048
e-mail: tnishio@east.ncc.go.jp

T. Nishio
Department of Radiology, Graduate School of Medicine, University of Tokyo, Tokyo, Japan

T. Inaniwa
Department of Energy Sciences, Tokyo Institute of Technology, Yokohama, Japan

K. Inoue
Functional Imaging Division, Research Center for Inovative Oncology, National Cancer Center, Kashiwa, Japan

A. Miyatake · T. Nishio
Department of Nuclear Engineering and Management, Graduate School of Engineering, University of Tokyo, Tokyo, Japan

K. Nakagawa
Department of Radiology, Faculty of Medicine, University of Tokyo, Tokyo, Japan

K. Yoda
Elekta K.K., Kobe, Japan

H_2O target and ^{11}C (half-life 20.4 min) in the CH_2 target were generated by photonuclear reactions.

Results. A comparison was made between measured activity and dose distributions for each target. The measured times of annihilation gamma rays from the positron emitter nucleus were 10 and 30 min for the ^{15}O nucleus in the H_2O target and the ^{11}C nucleus in the CH_2 target, respectively. The activity distributions of the ^{15}O and ^{11}C positron emitter nuclei were similar to the measured dose distributions for both depth and lateral directions except for dose buildup and collimator edge regions. It was confirmed that no activity was detected at an X-ray energy of 14 MV, which was far below the energy threshold for both photonuclear reactions.

Conclusion. It was estimated that the PET-CT image acquired from the activity of the ^{15}O and ^{11}C positron emitter nuclei might provide the area of X-ray beam irradiation in a phantom.

Key words High-energy photon therapy · Beam monitoring · Photonuclear reaction · PET-CT imaging

Introduction

The quality of radiotherapy largely depends on tumor dose conformity and patient positioning. Assessment of the conformal dose has been realized by rotational three-dimensional conformal radiation therapy (3D CRT)[1] and intensity-modulated radiation therapy (IMRT).[2] Intensity-modulated arc therapy (IMAT)[3] is regarded as a combination of 3D CRT and IMRT.

Accurate patient positioning prior to dose delivery has been achieved using millivolt CT,[4] in-room CT,[5] or kilovolt CT mounted on a linac gantry[6]; and radio-

therapy employing these accurate patient positioning methods is now called image-guided radiation therapy (IGRT). However, these IGRT techniques cannot fully ensure dose conformity to a moving tumor during treatment. Gated irradiation was proposed using an airbag sensor, CCD camera, laser sensor, and so on to monitor the patient's breathing cycle.[7-9] Recently, real-time embedded-marker detection using fluoroscopy[10] and real-time image correlation of 3D ultrasonographic images[11] were also proposed, with the objective of more accurate real-time tumor localization.

In the meantime, dose verification immediately after treatment was proposed using PET imaging of positron emitter nuclei generated in the target by a therapeutic irradiation beam. Simulation studies and experimental results were reported for charged ion treatment.[12-16] For high-energy photon treatment, the use of PET-CT at 50 MV was proposed; and experimental results[17-20] and Monte Carlo calculation results were also reported for in-beam PET imaging.[21]

The purpose of this article is to show that [15]O and ^{11}C positron emitter nuclei can be detected using a commercial PET-CT in the photonuclear reaction with X-ray energy as low as 21 MV. Furthermore, the PET-CT image obtained from such activity can provide the area of X-ray beam irradiation in a phantom.

Materials and methods

Photonuclear reactions by absorption of high-energy photons

When a high-energy photon reaches a nucleus, the photon is absorbed in the nucleus. If the excited states of the nucleus for the absorption of the energy have an energy higher than the binding energy of the nucleons, the nucleon goes outside the nucleus, thereby causing nuclear transmutation. The human body comprises carbon, nitrogen, oxygen, and hydrogen, and the main composition is carbon and oxygen.[22] For [16]O and ^{12}C nuclei, positron emitter nuclei of [15]O and ^{11}C are generated by X ray beams of energies exceeding 15.7 and 18.7 MeV, respectively. These are summarized in the following equations.

$$\begin{cases} {}^{16}O(\gamma,n)\,{}^{15}O\left({}^{+}\beta;T_{1/2}=122.2\sec\right) \\ {}^{12}C(\gamma,n)\,{}^{11}C\left({}^{+}\beta;T_{1/2}=20.4\min\right) \end{cases} \tag{1}$$

where $T_{1/2}$ is the half life of each positron emitter nucleus. The photonuclear reaction cross section at the energy of the incident photon[23] is shown in Fig. 1.
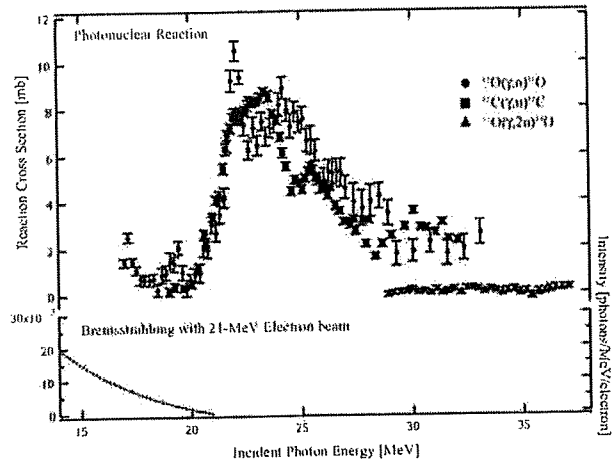

Fig. 1. Intensity of bremsstrahlung with a 21-MeV electron beam and photonuclear reaction cross section of [12]C(γ,n)[11]C, [16]O(γ,n)[15]O, and [16]O(γ,2n)[14]O at the energy of incident photons in the National Nuclear Data Center[21]

The intensity of a photon emitted from a tungsten target irradiated with a 21-MeV electron beam by bremsstrahlung, I, is calculated using Wu's approximation[24] of a radiation yield and is expressed as follows.

$$I[\text{photons/MeV/electron}] = 2.5\times10^{-2}\cdot\left\{4\cdot\left(1-\frac{E_x}{21}\right)+\frac{E_x}{7}\cdot\ln\left(\frac{E_x}{21}\right)\right\}. \tag{2}$$

where E_x is the energy of an X-ray by the bremsstrahlung. The calculation result is shown in Fig. 1.

High-energy photon beam to H_2O and CH_2 targets

The X-ray energy of 21 MV for the photonuclear reaction was generated by a microtron accelerator (Hitachi, HTM2200). H_2O and CH_2 targets were used previously for research of the photonuclear reaction in Eq. (1). The H_2O target was gelatinous water (99% pure water).[25] and the CH_2 target was high-density polyethylene. Each had dimensions of $10 \times 10 \times 40\,cm^3$. It should be noted that liquid water is not an appropriate phantom due to diffusion of the positron emitter nuclei. A dose of 17 Gy was delivered to each of the H_2O and CH_2 targets at the peak depth of 31 mm with a field size of $5 \times 5\,cm^2$ at the target surface. The X-ray beam was directed perpendicular to the $10 \times 10\,cm^2$ square surface with the beam axis centered on the square surface. The source-to-surface distance was 100 cm. and approximately 10 min were required to deliver 17 Gy. In addition, the percentage depth dose (PDD) and off-center ratio (OCR) were separately measured using a water phantom (CMS, Dynascan water phantom) and an ion chamber (0.125 cc, PTW 31005).

The positron emitter nuclei were not generated in the photonuclear reaction with an X-ray energy of 14 MV.

Activity measurement using PET-CT apparatus

PET-CT (GE, Discovery LS8) was used to measure 3D positron activity distributions, where 12096 BGO crystals were mounted having a dimension of $4 \times 8 \times 30$ mm^3. A 3D reconstruction algorithm of ordered subsets expectation maximization (OSEM) was employed with a transverse resolution of 4.8–5.2 mm and an axial resolution of 6.5–7.5 mm depending on the imaging position. The axial field of view (FOV) was 15.2 cm.

After dose delivery, the H_2O and CH_2 targets were moved to a PET-CT room. Measurement of the ^{16}O and ^{12}C activities was started 5 min after the irradiation. Each of the H_2O and CH_2 targets was positioned so the X-ray beam direction was parallel to the transverse imaging plane, thereby allowing full detection of all the annihilation gamma rays generated from the positrons (Fig. 2). At first, the PET-CT images of the ^{16}O and ^{12}C activities were reconstructed after 10-min annihilation gamma

counting. Subsequently, the counting time for CH_2 was extended to 30 min for more precise activity measurements in the depth and lateral directions. To derive a half-life for the H_2O target with 21-MV X-ray irradiation, the annihilation gammas were counted for every minute with a total measurement time of 10 min. For the CH_2 target with 21-MV irradiation, resulting annihilation gammas were counted for every 3 min with a total measurement time of 30 min. For 14-MV irradiation, annihilation gammas were always counted for every minute. The summary is shown in Table 1.

Results and discussion

Activity distributions in H_2O and CH_2 targets

Figure 3a shows a 3D PET-CT fusion image of a gelatinous water phantom (H_2O target), and Figure 3b depicts that of a polyethylene phantom (CH_2 target) after delivering a dose of 17 Gy with an X-ray beam energy of 21 MV. Each reconstructed 3D PET image along with
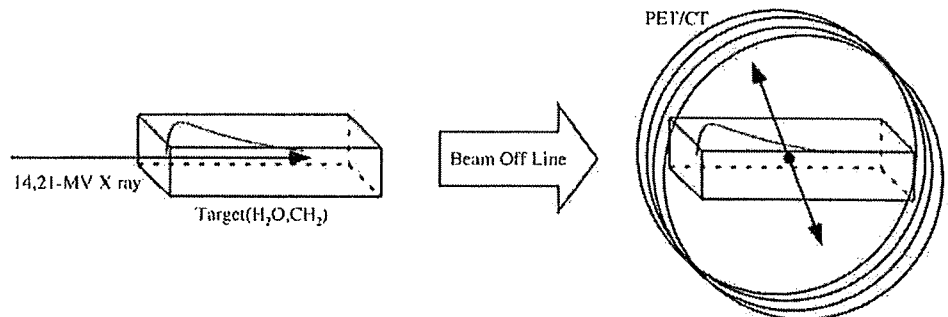
Fig. 2. Flow figure of X-ray irradiation to the target and measurement of annihilation gamma rays using a positron emission tomography-computed tomography (PET-CT) apparatus. The irradiated target was delivered from the irradiation room to the PET-CT room after X-ray irradiation (*Beam Off Line*). The target was positioned so the X-ray beam direction was parallel to the transverse imaging plane

Table 1. Condition of X-ray irradiation and activity measurement

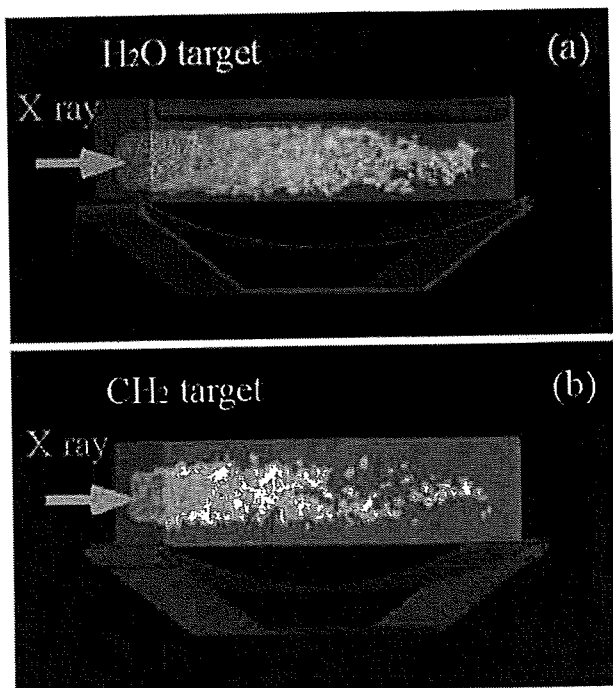| Target	Activity measurement (min)
Activity distribution (X-ray energy 21 MV; irradiation dose 17 Gy)	
H_2O	10
CH_2	10, 30
Decay curve	
X-ray energy 21 MV; irradiation dose 17 Gy	
H_2O	10 (1 × 10 times)
CH_2	30 (3 × 10 times)
X-ray energy 14 MV; irradiation dose 17 Gy	
H_2O	10 (1 × 10 times)
CH_2	10 (1 × 10 times)

Fig. 3. Three-dimensional PET-CT images of (a) a gelatinous water phantom (H_2O target) and (b) a polyethylene phantom (CH_2 target) after delivering a dose of 17 Gy with an X-ray beam energy of 21 MV. The activities of the PET images were the positron emitter nuclei of ^{15}O and ^{11}C from H_2O and CH_2 targets, respectively. Both PET images were reconstructed after 10 min of annihilation gamma counting

the fused CT image indicates that positron emitters were generated in each target. The detected total counts of annihilation gamma rays for the H_2O target were 478 494, and those for the CH_2 target were 129 843. The statistical error of the activity in each voxel unit of $0.0064 \, cm^3$ is about 20%.

Figure 4 shows comparisons between activity and dose distributions for the H_2O target with an annihilation gamma counting time of 10 min. Figure 4a represents depth distributions on the beam axis, where both activity and dose were normalized to 100 at a depth of 100 mm. The CT image profile is also shown. Figure 4b shows lateral distributions at a depth of 100 mm, where both activity and dose were normalized to 100 at the beam center. Figure 5 shows comparisons between activity and dose distributions for the CH_2 target with an annihilation gamma counting time of 30 min. Figure 5a represents depth distributions on the beam axis, where both activity and dose were normalized to 100 at a depth of 100 mm. The CT image profile is also shown. Figure 5b shows lateral distributions at a depth of 100 mm, where both activity and dose were normalized to 100 at the beam center. The statistical error of the activity in each 4-mm step of the lateral position is about 10%.

The reaction cross section of σ, which determines the rate of the generation, depends on the kind of the target nucleus (mass number of A_t, atomic number of Z_t) and the X-ray energy of E_X. The number of the positron emitter nuclei generated by the photonuclear reaction at each point $\vec{r}$, N_{net}, is given as follows.[16,25]

Fig. 4. Comparisons between activity and dose distributions for the H_2O target with an annihilation gamma counting time of 10 min. a Depth direction on the beam axis. Both activity and dose were normalized to 100 at a depth of 100 mm. A computed tomog-raphy (CT) image profile is also shown. b Lateral direction at a depth of 100 mm. Both activity and dose were normalized to 100 at the beam center
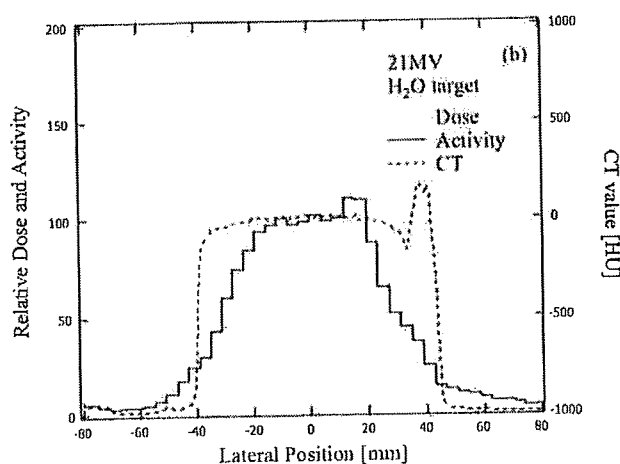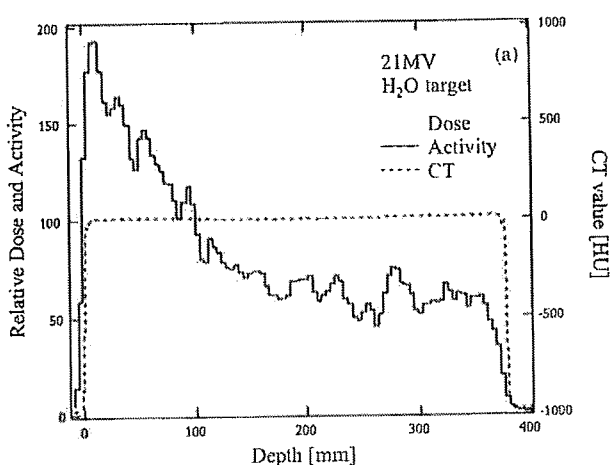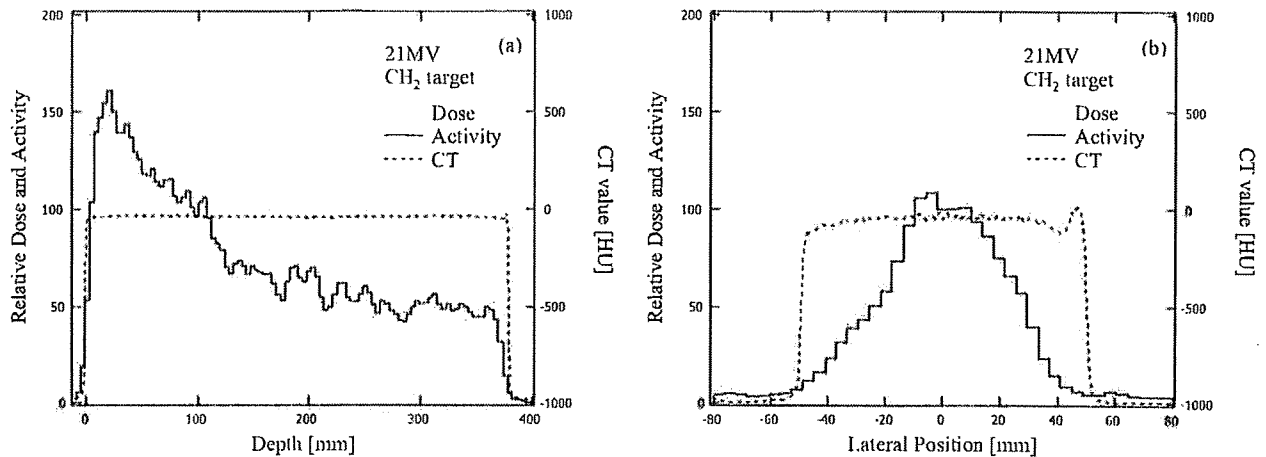
Fig. 5. Comparisons between activity and dose distributions for the CH_2 target with an annihilation gamma counting time of 30 min. a Depth direction on the beam axis. Both activity and dose were normalized to 100 at a depth of 100 mm. CT image profile is shown. b Lateral direction at a depth of 100 mm. Both activity and dose were normalized to 100 at the beam center

$$N_{act}(\vec{r},T_i,T_0,T_m,E_e,A_i,Z_i,n)$$

$$= \left[\int_{E_{th}}^{E_e} \left\{ \frac{d}{dE_x} F(\vec{r},E_X) \right\} \right.$$

$$\left. \times \sigma(E_X,A_i,Z_i) \cdot n(\vec{r},A_i,Z_i) \cdot \Delta(A_i,Z_i) dE_X \right] \qquad (3)$$

$$\times \left[\frac{T_{1/2}}{T_i \cdot \ln 2} \cdot \left(1 - 2^{-T_i/T_{1/2}}\right) \right] \times 2^{-T_0/T_{1/2}}$$

$$\times \left(1 - 2^{-T_m/T_{1/2}}\right) \cdot \varepsilon^2 \cdot \frac{\Omega_{PET}}{4 \cdot \pi}.$$

Here, F is the flux of the photon at each point $\vec{r}$. T_i denotes the time of the X-ray irradiation; T_0, the time between the completion of the X-ray irradiation and the start of PET measurement; T_m, the time of PET measurement; $T_{1/2}$, the half-life time of the positron emitter nuclei generated by the X-ray irradiation; ε, the detection efficiency at 511-keV single gamma ray; and Ω_{PET}, the total solid angle of the PET apparatus. E_{th} is the threshold energy for the photonuclear reaction; E_e, the energy of the incident electron beam for the bremsstrahlung; n, the number of target nuclei per volume; and Δ, the thickness of the target.

The relation between the X-ray dose and the activity distributions is expressed by Eq. (3).

$$\frac{N_{act}(\vec{r})}{D(\vec{r})} \propto \frac{\int_{E_{th}}^{E_e} \left\{ \frac{d}{dE_X} F(\vec{r},E_X) \right\} \cdot \sigma(E_X) \cdot n(\vec{r}) \cdot \Delta dE_X}{\int_0^{E_e} \left\{ \frac{d}{dE_X} F(\vec{r},E_X) \right\} \cdot TK(\vec{r},E_X) dE_X} \qquad (4)$$

Here, TK denotes the total X-ray energy deposited kernel. The X-ray energy deposition strongly depends on the secondary electrons by the primary photons. If the energy deposited kernel and the photonuclear reaction cross section are in proportion, the dose distribution form is similar to the activity distribution form.

Figures 4 and 5 suggest that the activity distribution is different from the dose distribution in the dose buildup and collimator edge regions. The dose distribution in the buildup regions is determined with the secondary electrons by the primary photons. However, the fluence of high-energy photons is significant for determining the activity distribution. For the depth activity and dose distributions, the fluence is maximum in the dose buildup region.[18] In addition, compared to the lateral dose distribution, the lateral activity distribution is anomalous in the collimator edge region; notably, it is significantly decreased at a larger off-axis distance for the CH_2 target. One possible interpretation of this is a reduction of mean X-ray energy due to collimator scattering in the collimator edge regions as well as the use of 21-MV beams with a higher energy threshold of 18.7 MeV for the photonuclear reaction of the ^{12}C nucleus.

Decay curve of activity for H_2O and CH_2 targets

Figure 6 shows decay curves of the total annihilation gamma counts detected by PET-CT as a function of time for H_2O and CH_2 targets at two X-ray energies: 21 MV and 14 MV. At 21 MV, curve-fitting functions for H_2O and CH_2 targets are given as follows.
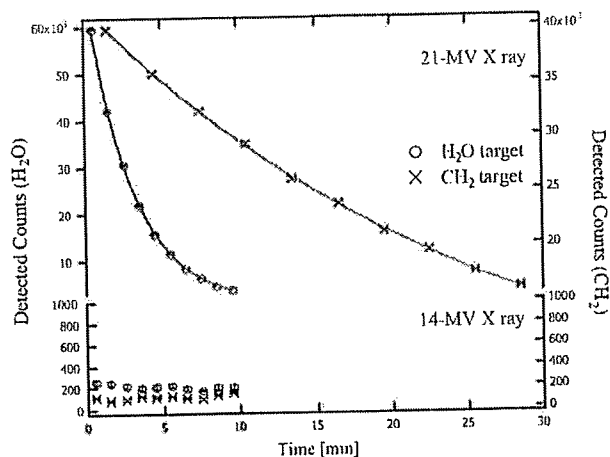
Fig. 6. Total annihilation gamma counts detected by PET-CT as a function of time for H_2O and CH_2 targets at two X-ray energies (21 MV and 14 MV). By way of curve fitting, the half-life for the H_2O target was found to be 122.5 s, which is in good agreement with the known half-life of ^{15}O. Similarly, the half-life for the CH_2 target was 18.8 min, which is also in good agreement with the known half-life of ^{11}C. No positron activity was detected at 14 MV

$$DC(T_m) \propto \begin{cases} 0.5^{T_m[\text{sec}]/122.5(\pm1.4)} : H_2O \\ 0.5^{T_m[\text{min}]/18.8(\pm0.7)} : CH_2 \end{cases} \qquad (5)$$

where DC stands for detection counts of annihilation gamma rays, and T_m is the time at measurement. The half-life for the H_2O target was 122.5 s, which is in good agreement with the known half-life of ^{15}O. The half-life for the CH_2 target was 18.8 min, which is also in good agreement with the known half-life of ^{11}C. At 14 MV, it was confirmed that no activity was detected.

In the present experiment, a dose of 17 Gy was required for PET image reconstruction. It is noted that 5 min were needed to move the phantom from the treatment room to the PET-CT room. During this period, the activity of ^{15}O reduces to 18% of the original activity owing to its short lifetime. If an on-line PET-CT was mounted to X-ray treatment equipment, a similar quality PET image along with a patient anatomy image could be obtained with a dose level of 3 Gy. It was estimated that on-beam line or in-irradiation room PET-CT imaging of ^{15}O positron emitter nuclei might provide the area of X-ray beam irradiation in a patient at a dose level of 3 Gy with X-ray beam energy of 21 MV.

Conclusions

The activity images of ^{15}O and ^{11}C positron emitter nuclei generated by 21-MV X-ray beam irradiation were able

to provide the beam monitoring in a phantom and in a patient's body in this study.

Currently, the photon energies used for radiotherapy are mostly 6 MV and 10 MV. However, it is suggested that radiotherapy with a higher energy X-ray beam is suitable for tumors in areas such as the prostate, pelvis, and large liver. Also, when a high dose per fraction is irradiated in hypofractionated radiotherapy, the treatment period can be reduced.[26] Beam monitoring systems are important for high accuracy in radiotherapy, and confirmation of the irradiation area in a patient becomes possible using a high-energy X-ray beam beyond the threshold energy for the photonuclear reaction. Highly accurate in-vivo dose control in patients is currently difficult, but further development of photonuclear reaction-based dosimetry may help achieve this goal.

References

1. Takabashi S. Conformation radiotherapy: rotation techniques as applied to radiography and radiotherapy of cancer Acta Radiol Suppl 1965;242:1.
2. Brahme A. Optimization of stationary and moving beam radiation therapy techniques. Radiother Oncol 1988;12:129–40.
3. Yu C. Intensity-modulated arc therapy with dynamic multileaf collimation: an alternative to tomotherapy. Phys Med Biol 1995;40:1435–49.
4. Simpson RG, Chen CT, Grubbs EA, Swindell W, A 4-MV CT scanner for radiation therapy: the prototype system. Med Phys 1982;9:574–9.
5. Aoki Y, Akanuma A, Karasawa K, Sakata K, Nakagawa K, Muta N, et al. An integrated radiotherapy treatment system and its clinical application Radiat Med 1987;5:131–41.
6. Jaffray DA, Siewerdsen JH, Wong JW, Martinez AA. Flat-panel cone-beam computed tomography for image-guided radiation therapy. Int J Radiat Oncol Biol Phys 2002;53:1337–49.
7. Ohara K, Okumura T, Akisada M, Inada T, Mori T, Yokota H, et al. Irradiation synchronized with respiration gate. Int J Radiat Oncol Biol Phys 1989;17:853–7.
8. Moore CH, Lilley F, Sauret V, Lalor M, Burton D. Optoelectronic sensing of body surface topology changes during radiotherapy for rectal cancer. Int J Radiat Oncol Biol Phys 2003;56:248–58.
9. Tsunashima Y, Sakae T, Shioyama Y, Kagei K, Terunuma T, Nohtomi A, et al. Correlation between the respiratory waveform measured using a respiratory sensor and 3D tumor motion in gated radiotherapy. Int J Radiat Oncol Biol Phys 2004;60:951–8.
10. Shirato H, Shimizu S, Shimizu T, Nishioka T, Miyasaka K. Real-time tumor-tracking radiotherapy. Lancet 1999;353:1331–2.
11. Sawada A, Yoda K, Kokubo M, Kunieda T, Nagata Y, Hiraoka M. A technique for noninvasive respiratory gated

radiation treatment system based on a real time 3D ultrasound image correlation: a phantom study. Med Phys 2004;31: 245–50.

12. Enghardt W, Fromm WD, Manfrass P, Schardt D. Limited angle 3D reconstruction of PET images for dose localization in light ion tumor therapy. Phys Med Biol 1992;37:791–8.

13. Litzenberg DW, Bajema JF, Becchetti FD, Brown JA, Raymond RS, Roberts DA, et al. On-line monitoring and PET imaging of proton radiotherapy beams. In: IEEE Medical Imaging Conference, Orlando, FL, 1992, pp 954–6.

14. Paans AMJ, Schippers JM. Proton therapy in combination with PET as monitor: a feasibility study. IEEE Trans Nucl Sci 1993;40:1041–4.

15. Litzenberg DW, Roberts DA, Lee MY, Pham K, Vander Molen AM, Ronningen R, et al. On-line monitoring of radiotherapy beams: experimental results with proton beams. Med Phys 1999;26:992–1006.

16. Nishio T, Ogino T, Nomura K, Uchida H. Dose-volume delivery guided proton therapy using beam on-line PET system. Med Phys 2006;33:4190–7.

17. Janek S. 3-Dimensional patient dose delivery verification based on PET-CT imaging of photonuclear reactions in 50 MV scanned photon beams. MSc thesis, Department of Medical Radiation Physics, Karolinska Institute and Royal Institute of Technology, 2002.

18. Brahme A. Biologically optimized 3-dimensional in vivo predictive assay-based radiation therapy using positron emission tomography-computerized tomography imaging. Acta Oncol 2003;42:123–36.

19. Uhrdin J, Janek S, Svensson R, Brahme A. 3D dose distribution in tissue calculated based on PET-CT imaging for high energy scanned photon therapy. Poster presentation, ESTRO, 2004.

20. Janek S. 3-Dimensional in vivo dose delivery verification by PET-CT imaging of photonuclear reactions in 50MV scanned photon beams. Series Internal Report, Department of Medical Radiation Physics, Karolinska Institute and Stockholm University, 2005, ISSN 1401-7466.

21. Muller H, Enghardt W. In-beam PET at high-energy photon beams. Phys Med Biol 2006;51:1779–89.

22. Photon, electron, proton and neutron interaction data for body tissues. ICRU Rep 1992;46:11–3.

23. National Nuclear Data Center, Brookhaven National Laboratory. Available at http://www.nndc.bnl.gov/.

24. Wu CS. The continuous X-rays excited by the beta-particles of ^{32}P. Phys Rev 1941;59:481–8.

25. Nishio T, Sato T, Kitamura H, Murakami K, Ogino T. Distributions of b^{+} decayed nuclei generated in the CH_2 and H_2O targets by the target nuclear fragment reaction using therapeutic MONO and SOBP proton beam. Med Phys 2005;32: 1070–82.

26. Abratt RP, Bogart JA, Hunter A. Hypofractionated irradiation for non-small cell lung cancer. Lung Cancer 2002;36: 225–33.

Contents lists available at ScienceDirect

Clinical Neurology and Neurosurgery
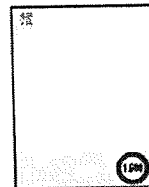
Spectroscopy-supported frame-based image-guided stereotactic biopsy of parenchymal brain lesions: Comparative evaluation of diagnostic yield and diagnostic accuracy

Mikhail F. Chernov [a,b,d,*], Yoshihiro Muragaki [b,d], Taku Ochiai [b], Takaomi Taira [b], Yuko Ono [c], Masao Usukura [c], Takashi Maruyama [b,d], Kotaro Nakaya [b], Ryoichi Nakamura [a,d], Hiroshi Iseki [a,b,d], Osami Kubo [b], Tomokatsu Hori [b], Kintomo Takakura [a,b,d]

[a] International Research and Educational Institute for Integrated Medical Sciences (IREIIMS), Tokyo Women's Medical University, Tokyo, Japan
[b] Department of Neurosurgery, Neurological Institute, Tokyo Women's Medical University, Tokyo, Japan
[c] Department of Neuroradiology, Neurological Institute, Tokyo Women's Medical University, Tokyo, Japan
[d] Faculty of Advanced Techno-Surgery, Institute of Advanced Biomedical Engineering and Science, Tokyo Women's Medical University, Tokyo, Japan

ARTICLE INFO

ABSTRACT

Objective: Comparative evaluation of diagnostic efficacy of stereotactic brain biopsy performed with and without additional use of spectroscopic imaging (^{1}H-MRS) for target selection was done.
Methods: From 2002 to 2006, 30 patients with parenchymal brain lesions underwent ^{1}H-MRS-supported frame-based stereotactic biopsy, whereas in 39 others MRI-guided technique was used. Comparison of diagnostic yield of the procedure in these two groups was performed. Additionally, the diagnostic accuracy was evaluated in 37 lesions, which were surgically resected within 1 month thereafter.
Results: Stereotactic biopsy permitted establishment of a definitive histopathological diagnosis in 57 cases and diagnosis of low-grade glioma without specific tumor typing in 8 cases. In 4 cases tissue sampling was non-diagnostic. In 5 out of 8 cases with incomplete diagnosis and in all non-diagnostic cases target selection was performed without the use of ^{1}H-MRS ($P = 0.2073$). The diagnostic yields of ^{1}H-MRS-supported and MRI-guided procedures were 100% and 90%, respectively ($P = 0.1268$). Comparison of the histopathological diagnoses after stereotactic biopsy and surgical resection revealed complete diagnostic agreement in 13 cases, minor disagreement in 14 cases, and major disagreement in 10 cases. Among these last 10 cases, initial undergrading of non-enhancing WHO grade III gliomas was the most common (7 cases). The diagnostic accuracy of ^{1}H-MRS-supported and MRI-guided procedures was 67% and 79%, respectively ($P = 0.4756$).
Conclusion: While in the present study the diagnostic yield of ^{1}H-MRS-supported frame-based stereotactic brain biopsy was 100%, its statistically significant diagnostic advantages over MRI-guided technique were not proved. Optimal selection of the spectroscopic target for tissue sampling remains unclear.
© 2009 Elsevier B.V. All rights reserved.

1. Introduction

Minimally invasive image-guided stereotactic biopsy is a routine neurosurgical procedure that provides an excellent opportunity to establish histopathological diagnosis of parenchymal brain lesions in virtually any location. Introduction of modern neuroimaging and development of computer-based techniques significantly facilitated target selection and navigation during tissue sam-

pling. Nevertheless, from 0.8% to 18.6% of stereotactic biopsies are considered non-diagnostic [1–14]. Moreover, even if histopathological diagnosis is provided, it can significantly differ from that determined after subsequent lesion resection. The rate of such discrepancy varies widely, from 3% to 49% [2,7,11,15–18].

The specific cause of diagnostic failure of stereotactic brain biopsy is the limitation of the structural neuroimaging in the evaluation of the lesion heterogeneity and subsequent suboptimal tissue sampling [8,19–26]. The use of metabolic information provided by positron emission tomography (PET) [18,19,22,24,27–33], single photon emission computed tomography (SPECT) [34], and spectroscopic imaging [20,35–45] for target selection can potentially result in improved diagnostic efficacy of the procedure. However, this has not been investigated in any controlled study. The objective of the present analysis was comparative evaluation of both

* Corresponding author at: International Research and Educational Institute for Integrated Medical Sciences (IREIIMS), Tokyo Women's Medical University, 8-1 Kawada-cho, Shinjuku-ku, Tokyo 162-8666, Japan. Tel.: +81 3 3353 8111x66003; fax: +81 3 5312 1844.
E-mail address: m.chernov@yahoo.com (M.F. Chernov).

diagnostic yield and diagnostic accuracy of the frame-based image-guided stereotactic biopsy of parenchymal brain lesions performed with and without additional use of metabolic data obtained with multivoxel proton magnetic resonance spectroscopy (^{1}H-MRS).

2. Materials and methods

From January 1, 2002 to December 31, 2006, 69 consecutive frame-based image-guided stereotactic biopsies of parenchymal brain lesions were performed in the Department of Neurosurgery of the Tokyo Women's Medical University. In 30 cases ^{1}H-MRS-detected metabolic information was used during target selection, whereas in 39 cases MRI-guided technique was utilized. The method of target selection (with or without the use of spectroscopic imaging) was determined by treating neurosurgeon according to his/her own preference, and no attempt of randomization was made. In both groups of patients, stereotactic biopsy was performed by two neurosurgeons (Drs. T. Ochiai and T. Taira), whereas tumor resection was done by three others (Drs. Y. Muragaki, T. Maruyama, and T. Hori).

One patient underwent stereotactic biopsy twice with an interval of 6 months, which was considered to be two separate cases. Low-grade astrocytoma was diagnosed after the initial MRI-guided procedure. The patient was followed without treatment, but due to rapid tumor progression the tissue sampling was repeated using ^{1}H-MRS support for target selection. At that time the diagnosis of glioblastoma was established. Another patient underwent a course of fractionated radiation therapy (total dose, 50 Gy) for suspected pontine glioma 15 months before stereotactic biopsy. All of the 66 other lesions were either previously untreated or unresponsive to conventional medical therapy, including steroids.

All data for the present analysis were extracted from the constantly maintained surgical, pathological, and radiological databases. For the purpose of the study all MRI and ^{1}H-MRS images were reviewed by a neurosurgeon and a neuroradiologist. Some cases from the same series had been analyzed separately and published previously elsewhere [46].

2.1. Clinical characteristics of patients

There were 45 males and 24 females. Their ages varied from 1 to 78 years (mean, 43 ± 19 years; median, 40 years). The series included 7 pediatric patients, but only one of them was less than 5 years old. According to the regulations of our hospital all patients were tested before surgery for human immunodeficiency virus (HIV), and no positive case was included in the present series.

There were 67 supratentorial and 2 infratentorial lesions. The predominant locations were the cerebral lobe (54 cases), basal ganglia and thalamus (11 cases), corpus callosum, pineal region, pons, and cerebellar hemisphere (1 case in each). Overall, 33 lesions were located on the left side, 32 on the right side, and 4 along the midline.

The majority of lesions (59 cases) had low intensity signal on T_1-weighted images, and high intensity signal on T_2-weighted images. A cyst-like structure of the lesion was noted in 3 cases only. Contrast enhancement was presented in 33 lesions, and was characterized as homogeneous in 8 cases, heterogeneous in 17, ring-like in 4, and patchy in 4.

Comparison of clinical and radiological variables in two groups of patients did not reveal statistically significant differences (Table 1).

2.2. Indications for stereotactic biopsy of parenchymal brain lesions

During the study period not more than 10% of the patients with parenchymal brain lesions underwent stereotactic biopsy in our clinic. The decision to perform tissue sampling was usually made by treating neurosurgeon and approved by the Chairman of the Department (Dr. T. Hori). The indications for the procedure included:

- clarification of the histopathological diagnosis, which could not be established based on clinical and radiological investigations, particularly for the differentiation of neoplastic and non-neoplastic lesions;
- histopathological confirmation of the diagnosis of the tumor, for which treatment with chemotherapy and/or irradiation was planned (for example, malignant lymphoma);
- stereotactic implantation of electrodes for preoperative brain mapping in the cases of gliomas; simultaneous sampling of the neoplasm was usually performed for the consideration of the rationale for its aggressive surgical resection.

Informed consent was obtained from each patient and/or his or her nearest family member. The protocol of ^{1}H-MRS-supported stereotactic brain biopsy was approved by responsible authorities of Tokyo Women's Medical University.

2.3. Neuroradiological guidance

On the day of treatment a Leksell G stereotactic frame (Elekta Instruments AB, Stockholm, Sweden) was fixed on the patient's head under local anesthesia, with the exception of a 1-year-old child, who was under general anesthesia during all stages of the procedure. Axial slices of the plain and contrast-enhanced CT, as well as axial slices of T_2-weighted MRI, and axial, coronal, and sagittal slices of T_1-weighted MRI before and after intravenous injection of single-dose (0.1 mmol/kg) gadoteridol (ProHance®; Eisai Co., Tokyo, Japan), were obtained through each 2 mm under stereotactic conditions. Cerebral angiography was performed in selected cases.

In cases of ^{1}H-MRS-supported stereotactic biopsy, a two-dimensional multivoxel long-echo (TR: 1500 ms, TE: 136 ms) volume-selected spectrum was acquired using double spin-echo acquisition mode, similar to point-resolved spectroscopy (PRESS). Axial postcontrast T_1-weighted MRI was mainly used as a scout image. Under three-dimensional control the ^{1}H-MRS voxel, separated by phase-encoding in 16 rectangular subvoxels (size 15 mm × 15 mm × 15 mm and volume 3.4 cm^3 each), was located on the maximal projection of the lesion. Spatial suppression pulses were applied to the outsides of the voxel to reduce spectral contamination. Global and localized shimming on the water proton and optimization of the water suppression were performed, resulting in water peak line widths of 2–4 Hz. Automatic spectral reconstruction with frequency referencing and application of the zero-level was achieved by software provided by the supplier (MRS-PRO/PX; Toshiba Medical Systems, Tokyo, Japan). Typically, time domain data were zero-filled to 4000 data points and multiplied with a Gaussian function, exponential line broadening was performed, two-dimensional Fourier transformation of the time domain signal into frequency domain signal was done, and baseline and zero-order phase corrections were applied. Metabolite signals from mobile lipids (Lip) [0.8 and 1.3 ppm], lactate (Lac) [1.3 ppm], N-acetylaspartate (NAA) [2.0 ppm], creatine and phosphocreatine (Cr) [3.0 ppm], and choline-containing compounds (Cho) [3.2 ppm] were obtained. Their peak intensity was calculated as an area under the curve. Thereafter, the metabolite ratio of NAA/Cho was calculated in each subvoxel and used for target selection. In the present study, the content of other identified metabolites, namely Lip, Lac, and Cr, was not taken into consideration during tissue sampling.

Both MRI and ^{1}H-MRS were acquired with a 1.5 T clinical imager (ExcellArt; Toshiba Medical Systems, Tokyo, Japan). A brain quadrature (QD) coil (Type MJQH107A-S1A; Toshiba Medical Systems)

Table 1
Clinical and radiological characteristics of cases in the present series.

Variables	All cases	Comparison of two investigated groups		
		MRI-guided technique (N = 39)	¹H-MRS-supported procedures (N = 30)	P-value
Patient age (years)				0.4593*
Median	40	42	38	
Range	1–78	1–72	12–78	
Patient gender				0.0688**
Men	45	29	16	
Women	24	10	14	
Predominant lesion location				0.3271**
Cerebral Lobe	54	29	25	
Basal ganglia/thalamus	11	7	4	
Others	4	3	1	
Lesion side				0.2543**
Left	33	21	12	
Right	32	16	16	
Midline	4	2	2	
Signal intensity of the lesion on MRI				0.6527**
Typical (low on T_1; high on T_2)	59	34	25	
Non-typical	10	5	5	
Contrast enhancement				0.1031**
Yes	33	22	11	
No	36	17	19	
Number of obtained tissue samples				0.6384***
1	39	23	16	
2	11	6	5	
3	7	2	5	
4	7	5	2	
5	2	1	1	
6	1	1	–	
7	1	1	–	
9	1	–	1	
Median	1	1	1	

N: number of cases.
* According to median test for two samples.
** According to chi-square test.
*** Comparison was done with chi-square test for cases with one vs. two and more obtained tissue samples.

was used. The spectroscopic examination usually required around 8 min.

2.4. Target selection and biopsy technique

All neuroradiological data were transferred for co-registration to Leksell GammaPlan version 2.0 or, later, Leksell SurgiPlan Release 2.20 (Elekta Instruments AB). Target selection was performed by reference to a simultaneous onscreen display of all obtained images. If biopsy was based on the structural neuroimaging alone, the contrast-enhanced part of the lesion, or its center, in cases of non-enhancing pathologies, was selected for tissue sampling. In cases of ¹H-MRS-supported biopsy the lesion-contained subvoxel with the lowest NAA/Cho ratio was identified and the contrast-enhanced part of the lesion within this area was selected as a target (Fig. 1). If the contrast-enhanced part of the lesion did not correspond to the ¹H-MRS subvoxel with the lowest NAA/Cho ratio, separate tissue specimens were obtained from each area. If contrast enhancement was absent, the center of the lesion was usually targeted, as well as the area corresponding to the ¹H-MRS subvoxel with the lowest NAA/Cho ratio. The actual value of the NAA/Cho ratio in the target in cases of ¹H-MRS-supported stereotactic biopsy varied from 0.04 to 1.38 (mean, 0.52 ± 0.37; median, 0.43).

All the procedures were performed under local anesthesia with additional intravenous sedation, except in the case of a 1-year-old child, who was operated on under general anesthesia. The supine position was used in all but one of the patients. Tissue samples were obtained with a Sedan-type blunt side-cutting aspiration biopsy

needle. Each histological specimen thus obtained was divided into two parts for intraoperative and permanent histopathological investigation, respectively. If the examination of the frozen biopsy sections did not determine the type of the pathological process, the tissue sampling was usually repeated using either the same or another target. The number of biopsy samples obtained did not differ significantly between two investigated groups of patients (Table 1).

2.5. Histopathological diagnosis

Final histopathological diagnosis was established on the formalin-fixed paraffin-embedded tissue sections. It was considered to be (Table 2):

- definitive, if both type and grade of the tumor or nature of the non-neoplastic pathological process was defined;
- incomplete, if neoplastic pathology was determined, but its precise type and/or grade remained unclear;
- non-diagnostic, if histopathological findings were non-specific and did not permit establishment of a diagnosis of the lesion.

The neuropathologist was fully informed about the clinical history, radiological characteristics of the lesion, and target positioning. Grading and typing of tumors was based on the World Health Organization (WHO) criteria and was retrospectively adapted to its latest requirements [47]. For the diagnosis of oligoastrocytoma the presence of both astrocytic and oligodendroglial components should
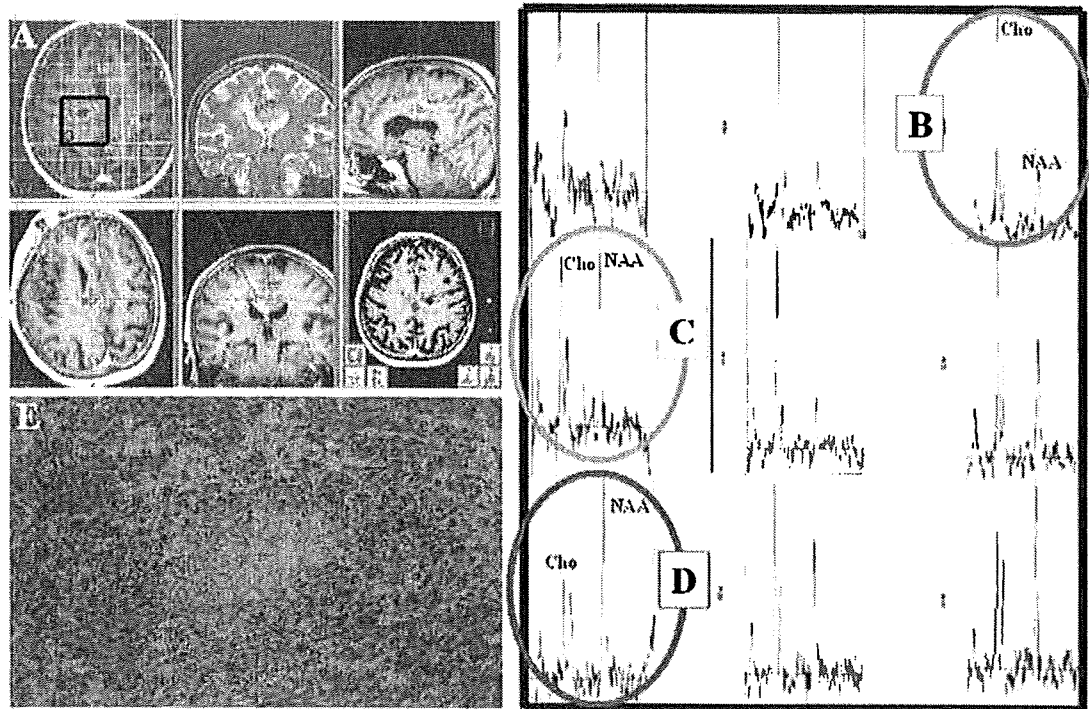
Fig. 1. Spectroscopy-supported stereotactic biopsy of the right-sided fronto-parietal tumor: ^{1}H-MRS scout image and MR images were co-registered in Leksell SurgiPlan (A), spectrum with the lowest NAA/Cho ratio (0.34) was identified (B), and contrast-enhanced part of the lesion within this area was targeted. Less significant metabolic alterations (NAA/Cho ratio 1.03) in the lesion-contained subvoxel (C) and practically normal [1]H-MR spectrum (NAA/Cho ratio 1.98) in the vicinity to the neoplasm (D) are shown for comparison. The histopathological examination revealed glioblastoma multiforme (E). Peaks of N-acetylaspartate (NAA) and choline-containing compounds (Cho) are marked.

constitute not less than 25% [48]; otherwise a diagnosis of glioma with specific cell component was made.

2.6. Further treatment

In 37 cases (18 after ^{1}H-MRS-supported stereotactic biopsy and 19 after MRI-guided procedures), microsurgical excision of the lesion was performed within a month (on average, in 2 ± 1 weeks) after initial tissue sampling. In the vast majority of gliomas, more than 80% resection was attained according to our policy of their aggressive surgical management [49].

Histopathological diagnosis of the lesion after craniotomy was established on the formalin-fixed paraffin-embedded tissue sections of all obtained pathological material, without specific investigation of the area sampled during initial stereotactic biopsy. Diagnostic agreement was considered as [11]:

- complete, if final histopathological diagnoses after both procedures were identical;
- minor disagreement, if final histopathological diagnoses after both procedures were slightly different, but without significant impact on the treatment strategy and prognosis;
- major disagreement, if histopathological diagnoses after both procedures differed significantly, which could have a serious impact on the choice of the appropriate management and determination of prognosis.

2.7. Statistics

The chi-square test, the median test for two samples, and Fisher's exact test were used for data analysis. The level of significance was determined at $P < 0.05$.

3. Results

3.1. Complications

One patient in the present series had an intratumoral hemorrhage immediately after stereotactic biopsy of malignant lymphoma based solely on structural neuroimaging. This necessitated microsurgical removal of the neoplasm and blood clot, and, overall, resulted in significant neurological disability. No other cases of major postoperative complications occurred.

3.2. Intraoperative histopathological diagnosis

In 62 cases (90%) the type of the pathological process, namely tumor (with or without more detailed typing and/or grading), cerebral infarction, acute inflammation, and multiple sclerosis, was determined on the intraoperative frozen tissue sections. This rate did not differ significantly between cases with and without the use of ^{1}H-MRS for target selection (28 out of 30 cases [93%] vs. 34 out of 39 cases [87%]; $P = 0.6905$).

In 7 cases (10%) only non-specific histopathological findings were disclosed during intraoperative investigation. In 5 of these cases ^{1}H-MRS-detected metabolic information was not used for target selection. In 3 cases with non-specific findings on the frozen sections, including both after ^{1}H-MRS-supported stereotactic biopsy, further examination of the permanent tissue sections permitted establishment of incomplete diagnosis of low-grade glioma, whereas 4 others remained non-diagnostic. Nevertheless, the association between the use of metabolic data for target selection and establishment of the histopathological diagnosis on permanent tissue sections in cases with unclear intraoperative diagnosis on frozen sections did not reach the level of statistical significance ($P = 0.1429$).

Table 2

Final histopathological diagnosis established on tissue samples obtained with stereotactic brain biopsy in the present series.

Histopathological diagnosis	Number of cases		
	All cases	MRI-guided technique	1H-MRS-supported procedures
Definitive diagnosis			
WHO grade II tumors	28 (40.6%)	14 (35.9%)	14 (46.7%)
Pleomorphic xanthoastrocytoma	1	1	–
Fibrillary astrocytoma	8	5	3
Fibrillary astrocytoma with pilocytic component	1	1	–
Fibrillary astrocytoma with gemistocytic component	1	–	1
Gemistocytic astrocytoma	1	1	–
Diffuse astrocytoma with oligodendroglial component	1	–	1
Diffuse astrocytoma (not other specified)	4	1	3
Oligodendroglioma	5	3	2
Oligodendroglioma with astrocytic component	1	–	1
Oligoastrocytoma	5	2	3
WHO grade III tumors	6 (8.7%)	2 (5.1%)	4 (13.3%)
Anaplastic astrocytoma	3	1	2
Anaplastic astrocytoma with oligodendroglial component	1	–	1
Anaplastic oligodendroglioma	1	–	1
Anaplastic oligoastrocytoma	1	1	–
WHO grade IV tumors	18 (26.1%)	11 (28.2%)	7 (23.3%)
Glioblastoma	7	3	4
Malignant lymphoma	7	5	2
Germinoma	2	1	1
Metastatic carcinoma	2	2	–
Non-neoplastic pathology	5 (7.2%)	3 (7.7%)	2 (6.7%)
Encephalitis	2	1	1
Old cerebral infarction	1	1	–
Multiple sclerosis	2	1	1
Incomplete diagnosis			
Low-grade glioma	8 (11.6%)	5 (12.8%)	3 (10.0%)
Non-diagnostic cases	4 (5.8%)	4 (10.3%)	–
Satellitosis and peritumoral brain	1	1	–
Normal brain tissue with fibrous meningothelial part	1	1	–
Gliofibrillary tissue with necrosis and lymphoid cell infiltration	1	1	–
Chronic inflammation with demyelination	1	1	–
Total number of cases	69 (100%)	39 (100%)	30 (100%)

WHO: World Health Organization.

3.3. Final histopathological diagnosis and diagnostic yield

In 57 cases (83%), a definitive histopathological diagnosis was established on the permanent tissue sections. This rate did not differ significantly between cases with and without the use of 1H-MRS for target selection (27 out of 30 cases [90%] vs. 30 out of 39 cases [77%]; $P = 0.2073$).

In 8 patients (11%), incomplete diagnosis of low-grade glioma without precise tumor typing and/or grading was performed. In 4 other patients (6%) the histopathological findings on the permanent tissue sections were non-specific and did not permit establishment of a diagnosis of the lesion (Table 3). In 5 out of 8 cases with incom-

plete final histopathological diagnosis, and in all non-diagnostic cases, 1H-MRS-detected metabolic data were not used for target selection.

Overall the diagnostic yield of stereotactic biopsy in the present series was 94% (65 out of 69 cases). It was 100% (30 out of 30 cases) in 1H-MRS-supported procedures, compared to 90% (35 out of 39 cases) in MRI-guided tissue sampling ($P = 0.1268$).

3.4. Diagnostic accuracy

Comparison of the histopathological diagnoses after stereotactic biopsy and surgical resection in 37 patients who underwent lesion

Table 3

Non-diagnostic cases of stereotactic brain biopsy in the present series.

Case no.	Age, sex	Number of biopsy samples	Diagnosis after stereotactic biopsy	Diagnosis after surgical resection	Contrast enhancement	1H-MRS support
1	65, M	2	Satellitosis and peritumoral brain	Anaplastic oligodendroglioma WHO grade III	No	No
2	16, M	2	Normal brain tissue with fibrous meningothelial part	Focal cortical dysplasia	No	No
3	42, M	4	Gliofibrillary tissue with necroses and lymphoid cell infiltration	Old cerebral infarction	Patchy	No
4	51, M	4	Chronic inflammation and demyelination	Surgery was not done	Patchy	No

M, male; F, female.

removal within a month after initial tissue sampling revealed complete diagnostic agreement in 13 cases (35%). Minor disagreement was noted in 14 cases (38%) and at least one of the following diagnostic errors after stereotactic biopsy was included: designation of WHO grade I tumors as grade II; incomplete histopathological diagnosis or erroneous typing of gliomas with their exact grading; missed diagnosis of the focal cortical dysplasia and old cerebral infarction. Major diagnostic disagreement was noted in 10 cases (27%). Among these 10 cases, initial undergrading of non-enhancing WHO grade III gliomas was the most common (Table 4).

Overall the diagnostic accuracy of stereotactic biopsy in the present series was 73% (27 out of 37 cases). It was 67% (12 out of 18 cases) in ^{1}H-MRS-supported procedures, compared to 79% (15 out of 19 cases) in MRI-guided tissue sampling ($P = 0.4756$).

In 27 cases (73%), the MIB-1 index established at the time of stereotactic biopsy was within the 95% confidence interval of those that was determined after resection of the lesion. This rate did not differ significantly between cases with and without the use of ^{1}H-MRS for target selection (14 out of 18 cases [78%] vs. 13 out of 19 cases [68%]; $P = 0.7140$).

4. Discussion

Targeting in cases of image-guided stereotactic brain biopsy is usually directed on the contrast-enhanced part of the lesion, or on its center, if contrast enhancement is absent [3,50,51]. Possible heterogeneity of the neoplasm, however, creates intrinsic diagnostic limitations for the procedure. Particularly, undergrading of gliomas is not uncommon [1,2,7,16–18]. In the series of Jackson et al. [7], 63% of tumors initially classified as of low or intermediate grade and 60% of anaplastic astrocytomas were found to be more malig-

nant after subsequent surgical resection. Proposed multiple tissue sampling from different parts of the lesion can improve the diagnostic accuracy of stereotactic biopsy [17,50,51]. However, it may be associated with increased risk of major regional complications and neurological deterioration, especially if performed in the eloquent brain areas [22,31].

Additional use of metabolic data for target selection can potentially increase the diagnostic efficacy of stereotactic brain biopsy. Previous reports noted significant improvement of its diagnostic yield if guidance with ^{18}F-fluorodeoxyglucose, L-methyl-^{11}C-methionine, O-2-^{18}F-fluoroethyl-L-tyrosine, ^{18}F-choline and ^{11}C-choline PET [19,22,24,27–33], or [201]thallium SPECT [34] was used. These techniques, however, have recognizable disadvantages, such as radiation exposure, excessive time requirements, poor anatomical resolution, technological complexity, and financial expense, which limit their possible use to highly specialized centers [22,24,34,44].

Alternatively, ^{1}H-MRS is a completely non-invasive, extremely sensitive, and highly informative investigation, which can be easily attained at the time of routine MRI. The content of ^{1}H-MRS-detected metabolites reflects certain pathophysiological processes in the investigated volume of tissue [42,43,52–59]. Acquisition of spectroscopic images before planned stereotactic brain biopsy does not require any special equipment and is not accompanied by a significant increase in examination time. Spectroscopic data can be easily incorporated into a computer-based program for neuronavigation. Technical simplicity facilitates routine use of ^{1}H-MRS-support during image-guided stereotactic procedures and there are multiple reports on its effective use for metabolically guided lesion resection [60,61] or biopsy [20,35–42,44,62].

In the present series, the diagnostic yield of ^{1}H-MRS-supported stereotactic tissue sampling was 100%, which is in concordance with

Table 4

Cases with major disagreement of the histopathological diagnoses established after stereotactic biopsy and subsequent surgical resection of the lesion.

Case no.	Age, sex	Number of biopsy samples	Diagnosis after stereotactic biopsy	Diagnosis after surgical resection	Contrast enhancement	^{1}H-MRS support[a]
1	33, M	1	Oligodendroglioma WHO grade II	Anaplastic oligodendroglioma WHO grade III	No	No
2	26, M	1	Fibrillary astrocytoma WHO grade II	Anaplastic astrocytoma with gemistocytic component WHO grade III	Heterogeneous	No
3	54, F	1	Diffuse astrocytoma (not other specified) WHO grade II	Anaplastic oligodendroglioma with astrocytic component WHO grade III	No	No
4	30, M	1	Diffuse astrocytoma (not other specified) WHO grade II	Anaplastic astrocytoma with gemistocytic component WHO grade III	No	Yes (0.56)
5	27, M	1	Diffuse astrocytoma (not other specified) WHO grade II	Anaplastic oligodendroglioma WHO grade III	No	Yes (0.21)
6	58, M	1	Fibrillary astrocytoma with gemistocytic component WHO grade II	Anaplastic astrocytoma WHO grade III	No	Yes (0.30)
7	37, F	2	Oligoastrocytoma WHO grade II	Anaplastic astrocytoma with oligodendroglial component WHO grade III	No	Yes (0.40)
8	32, M	4	Oligoastrocytoma WHO grade II	Anaplastic oligoastrocytoma WHO grade III	No	Yes (0.04)
9	38, M	5	Anaplastic astrocytoma WHO grade III	Oligodendroglioma with astrocytic component WHO grade II	No	Yes (0.72)
10	65, M	2	Satellitosis and peritumoral brain	Anaplastic oligodendroglioma WHO grade III	No	No

M, male; F, female.

Note that Case 10 corresponds to Case 1 in Table 3.

[a] Exact values of NAA/Cho ratio in the target are presented in parentheses.

previous reports on ^{1}H-MRS-guided [35–37,41,44], PET-guided [19,22,29–31], and perfusion-weighted MRI-guided [23] biopsies. However, the difference compared to procedures based solely on structural neuroimaging did not reach the level of statistical significance, probably due to the high diagnostic efficacy of the MRI-guided biopsy itself and the relatively small number of cases in the present series. Moreover, ^{1}H-MRS support was not associated with improved diagnostic accuracy when lesions surgically resected after initial tissue sampling were analyzed separately. This could be caused by incomplete coverage of the tumor with two-dimensional ^{1}H-MRS voxel, a relatively large size of subvoxels, or suboptimal selection of the metabolic target.

Typical ^{1}H-MRS-detected metabolic abnormalities in brain tumors include increase of Cho, decreases of NAA and Cr, and frequent appearance of Lac and Lip [14,21,43,52,56,58,62]. Cho is associated with both synthesis and degradation of cell membranes, and its increase may reflect high cellularity, active proliferation, inflammation, or early necrotic processes. NAA is nearly selectively distributed in neurons, and reflects their density, viability, and functional activity. It was shown previously that increase of proliferative activity and malignant progression of parenchymal brain tumors are generally correlated with increase of Cho and Lip contents and decrease of NAA content, while some highly malignant neoplasms with extensive necroses may have lower Cho content compared to their more benign counterparts [42,43,52–59]. In a clinical setting, the content of metabolites is usually expressed semiquantitatively as various metabolic ratios. The NAA/Cho ratio, which was used in the present series for the selection of the target for stereotactic biopsy, is a validated marker of the tumor presence, proliferative activity, and growth characteristics [20,24,38–40,42,52,53,57,63]. In our own retrospective analysis of various ^{1}H-MRS-detected metabolic parameters in differentiation of 71 high-grade and low-grade gliomas, the NAA/Cho ratio showed the strongest discriminative power [64]. Nevertheless, it may be not specific enough for precise determination of the histopathological tumor grade in each individual case [24,52,57,63]. Recently, Ng and Lim [45] showed that direction of the tissue sampling on the area with the lowest NAA/Cho might lead to erroneous diagnosis of anaplastic astrocytoma in cases of glioblastomas. In concordance with their report, the results presented herein permit us to conclude that tissue sampling from the area of the lowest NAA/Cho ratio may result in undergrading of the non-enhancing WHO grade III gliomas. This was observed in 5 out of 6 cases with major diagnostic errors after ^{1}H-MRS-supported stereotactic brain biopsy in the present series (Table 4).

Other metabolic targets for ^{1}H-MRS-guided tissue sampling have been used previously. McKnight et al. [42] recommended selection of the biopsy target based both on the maximal value of Cho/NAA ratio and the originally developed Cho-to-NAA index, which reflects the number of standard deviations of difference between the relative level of Cho in a given voxel and the mean relative level of Cho in voxels from non-tumor regions. In a limited number of patients Son et al. [37] obtained tissue samples from the areas of increased Cho/Cr, decreased NAA/Cr and elevated Lac signal, and found good histopathological correspondence in all cases. In 26 patients with parenchymal brain tumors, including 16 after previous irradiation, Martin et al. [36] directed the biopsy on the area of highest Cho signal intensity compared to its level in the normal brain. It was effective in 17 out of 21 histologically confirmed tumors, but four malignant neoplasms did not exhibit elevation of Cho, which precluded their definitive metabolic targeting. Hermann et al. [44] used a similar technique with a 3 T MR scanner and attained 89% diagnostic accuracy in discrimination between non-enhancing WHO grade II and grade III gliomas. In 2 cases of malignant gliomas, Ng and Lim [45] advocated tissue sampling from the area with the highest Lip content. Neverthe-

less, direct comparison of the histopathological diagnoses obtained with ^{1}H-MRS-supported stereotactic biopsy and subsequent surgical resection of the lesion was not performed in any previous study.

While advantages of ^{1}H-MRS-supported tissue sampling over MRI-guided technique were not statistically proved in the present study, some indications for metabolic guidance during stereotactic brain biopsies may be considered reasonable. First, it may be extremely helpful in lesions progressing after irradiation, with frequent co-existence of radiation-induced necrosis and viable neoplasm [36,38,39,41,43,62,63,65]. Second, detection of the metabolic abnormalities outside the contrast-enhanced area of the highly vascular tumor can make it possible to obtain a representative tissue specimen with reduced risk of hemorrhagic complications [51,63]. Further testing of other ^{1}H-MRS-detected parameters, particularly the evaluation of the relative content of Lip and pattern analysis of the pathological spectrum [45,64], may facilitate optimal selection of the metabolic target for tissue sampling. Finally, introduction of MR scanners with high magnetic field strength (3 T and more) for spectroscopic imaging can provide an opportunity to use smaller voxel size with good signal-to-noise ratio, acceptable acquisition time, and better spectral resolution, which may result in more precise navigation of stereotactic brain biopsy [44].

5. Conclusion

In the present series, the use of ^{1}H-MRS-support for frame-based image-guided stereotactic biopsy of parenchymal brain lesions resulted in 100% diagnostic yield and 67% diagnostic accuracy. These parameters, however, did not differ significantly from an MRI-based technique. Further search for optimal metabolic targets is necessary for the improvement of the diagnostic efficacy of spectroscopic navigation during tissue sampling, particularly in cases of non-enhancing intermediate grade gliomas.

Acknowledgements

References

[1] Blaauw G, Braakman R. Pitfalls in diagnostic stereotactic brain surgery. Acta Neurochir Suppl 1988;42:161–5.

[2] Voges J, Schroder R, Treuer H, Pastyr O, Schlegel W, Lorenz WJ, et al. CT-guided and computer assisted stereotactic biopsy: technique, results, indications. Acta Neurochir (Wien) 1993;125:142–9.

[3] Soo TM, Bernstein M, Provias J, Tasker R, Lozano A, Guha A. Failed stereotactic biopsy in a series of 518 cases. Stereotact Funct Neurosurg 1996;64:183–96.

[4] Hall WA. The safety and efficacy of stereotactic biopsy for intracranial lesions. Cancer 1998;82:1749–55.

[5] Fontaine D, Dormont D, Hasboun D, Clemenceau S, Valery C, Oppenheim C, et al. Magnetic resonance-guided stereotactic biopsies: results in 100 consecutive cases. Acta Neurochir (Wien) 2000;142:249–56.

[6] Yu X, Liu Z, Tian Z, Li S, Huang H, Xiu B, et al. Stereotactic biopsy for intracranial space-occupying lesions: clinical analysis of 550 cases. Stereotact Funct Neurosurg 2000;75:103–8.

[7] Jackson RJ, Fuller GN, Abi-Said D, Lang FF, Gokaslan ZL, Shi WM, et al. Limitations of stereotactic biopsy in the initial management of gliomas. Neurooncology 2001;3:193–200.

[8] Kim JE, Kim DG, Paek SH, Jung HW. Stereotactic biopsy for intracranial lesions: reliability and its impact on the planning of treatment. Acta Neurochir (Wien) 2003;145:547–55.

[9] Takahashi H, Sugai T, Uzuka T, Kano M, Honma J, Grinev I, et al. Complications and diagnostic yield of stereotactic biopsy for the patients with malignant brain tumors. No Shinkei Geka 2004;32:135–40 (in Japanese).

[10] Yamada K, Goto S, Kochi M, Ushio Y. Stereotactic biopsy for multifocal, diffuse, and deep-seated brain tumors using Leksell's system. J Clin Neurosci 2004;11:263–7.

[11] Aker FV, Hakan T, Karadereler S, Erkan M. Accuracy and diagnostic yield of stereotactic biopsy in the diagnosis of brain masses: comparison of results of biopsy and resected surgical specimens. Neuropathology 2005;25:207–13.

[12] Heper AO, Erden E, Savas A, Ceyhan K, Erden I, Akyar S, et al. An analysis of stereotactic biopsy of brain tumors and nonneoplastic lesions: a prospective clinicopathologic study. Surg Neurol 2005;64(Suppl. 2):S82–8.

[13] Jain D, Sharma MC, Sarkar C, Deb P, Gupta D, Mahapatra AK. Correlation of diagnostic yield of stereotactic brain biopsy with number of biopsy bits and site of the lesion. Brain Tumor Pathol 2006;23:71–5.

[14] Setzer M, Herminghaus S, Marquardt G, Tews DS, Pilatus U, Seifert V, et al. Diagnostic impact of proton MR-spectroscopy versus image-guided stereotactic biopsy. Acta Neurochir (Wien) 2007;149:379–86.

[15] Kleihues P, Volk B, Anagnostopoulos J, Kiessling M. Morphologic evaluation of stereotactic brain tumour biopsies. Acta Neurochir Suppl 1984;33:171–81.

[16] Chandrasoma PT, Smith MM, Apuzzo MLJ. Stereotactic biopsy in the diagnosis of brain masses: comparison of results of biopsy and resected surgical specimen. Neurosurgery 1989;24:160–5.

[17] Feiden W, Steude U, Bise K, Gundisch O. Accuracy of stereotactic brain tumor biopsy: comparison of the histologic findings in biopsy cylinders and resected tumor tissue. Neurosurg Rev 1991;14:51–6.

[18] McGirt MJ, Villavicencio AT, Bulsara KR, Friedman AH. MRI-guided stereotactic biopsy in the diagnosis of glioma: comparison of biopsy and surgical resection specimen. Surg Neurol 2003;59:277–82.

[19] Levivier M, Goldman S, Pirotte B, Brucher JM, Baleriaux D, Luxen A, et al. Diagnostic yield of stereotactic brain biopsy guided by positron emission tomography with [18F]fluorodeoxyglucose. J Neurosurg 1995;82:445–52.

[20] Croteau D, Scarpace L, Hearshen D, Gutierrez J, Fisher JL, Rock JP, et al. Correlation between magnetic resonance spectroscopy imaging and image-guided biopsies: semiquantitative and qualitative histopathological analyses of patients with untreated glioma. Neurosurgery 2001;49:823–9.

[21] Law M, Yang S, Wang H, Babb JS, Johnson G, Cha S, et al. Glioma grading: sensitivity, specificity, and predictive values of perfusion MR imaging and proton MR spectroscopic imaging compared with conventional MR imaging. AJNR Am J Neuroradiol 2003;24:1989–98.

[22] Pirotte B, Goldman S, Salzberg S, Wikler D, David P, Vandesteene A, et al. Combined positron emission tomography and magnetic resonance imaging for the planning of stereotactic brain biopsies in children: experience in 9 cases. Pediatr Neurosurg 2003;38:146–55.

[23] Maia Jr ACM, Malheiros SMF, da Rocha AJ, Stavale JN, Guimaraes IF, Borges LRR, et al. Stereotactic biopsy guidance in adults with supratentorial nonenhancing gliomas: role of perfusion-weighted magnetic resonance imaging. J Neurosurg 2004;101:970–6.

[24] Floeth FW, Pauleit D, Wittsack H-J, Langen KJ, Reifenberger G, Hamacher K, et al. Multimodal metabolic imaging of cerebral gliomas: positron emission tomography with [18F]fluoroethyl-L-tyrosine and magnetic resonance spectroscopy. J Neurosurg 2005;102:318–27.

[25] Maia ACM, Malheiros SMF, da Rocha AJ, da Silva CJ, Gabbai AA, Ferraz FAP, et al. MR cerebral blood volume maps correlated with vascular endothelial growth factor expression and tumor grade in nonenhancing gliomas. AJNR Am J Neuroradiol 2005;26:777–83.

[26] Rollin N, Guyotat J, Streichenberger N, Honnorat J, Tran Minh V-A, Cotton F. Clinical relevance of diffusion and perfusion magnetic resonance imaging in assessing intra-axial brain tumors. Neuroradiology 2006;48:150–9.

[27] Hanson MW, Glantz MJ, Hoffman JM, Friedman AH, Burger PC, Schold SC, et al. FDG-PET in the selection of brain lesions for biopsy. J Comput Assist Tomogr 1991;15:796–801.

[28] Levivier M, Goldman S, Bidaut L, Luxen A, Stanus E, Przedborski S, et al. Proton emission tomography-guided stereotactic brain biopsy. Neurosurgery 1992;31:792–7.

[29] Maciunas RJ, Kessler RM, Maurer C, Mandava V, Watt G, Smith G. Positron emission tomography imaging-directed stereotactic neurosurgery. Stereotact Funct Neurosurg 1992;58:134–40.

[30] Pirotte B, Goldman S, David P, Wikler D, Damhaut P, Vandesteene A, et al. Stereotactic brain biopsy guided by positron emission tomography (PET) with [F-18]fluorodeoxyglucose and [C-11]methionine. Acta Neurochir Suppl 1997;68:133–8.

[31] Massager N, David P, Goldman S, Pirotte B, Wikler D, Salmon I, et al. Combined magnetic resonance imaging- and positron emission tomography-guided stereotactic biopsy in brainstem mass lesions: diagnostic yield in a series of 30 patients. J Neurosurg 2000;93:951–7.

[32] Messing-Junger AM, Floeth FW, Pauleit D, Reifenberger G, Willing R, Gartner J, et al. Multimodal target point assessment for stereotactic biopsy in children with diffuse bithalamic astrocytomas. Childs Nerv Syst 2002;18:445–9.

[33] Hara T, Kondo T, Hara T, Kosaka N. Use of 18F-choline and 11C-choline as contrast agents in positron emission tomography imaging-guided stereotactic biopsy sampling of gliomas. J Neurosurg 2003;99:474–9.

[34] Hemm S, Vayssiere N, Zanca M, Ravel P, Coubes P. Thallium SPECT-based stereotactic targeting for brain tumor biopsies. Stereotact Funct Neurosurg 2004;82:70–6.

[35] Hall WA, Martin A, Liu H, Truwit CL. Improving diagnostic yield in brain biopsy: coupling spectroscopic targeting with real-time needle placement. J Magn Reson Imaging 2001;13:12–5.

[36] Martin AJ, Liu H, Hall WA, Truwit CL. Preliminary assessment of turbo spectroscopic imaging for targeting in brain biopsy. AJNR Am J Neuroradiol 2001;22:959–68.

[37] Son BC, Kim MC, Choi BG, Kim EN, Baik HM, Choe BY, et al. Proton magnetic resonance chemical shift imaging (1H CSI)-directed stereotactic biopsy. Acta Neurochir (Wien) 2001;143:45–50.

[38] Rock JP, Hearshen D, Scarpace L, Croteau D, Gutierrez J, Fisher JL, et al. Correlations between magnetic resonance spectroscopy and image-guided histopathology, with special attention to radiation necrosis. Neurosurgery 2002;51:912–20.

[39] Rock JP, Scarpace L, Hearshen D, Gutierrez J, Fisher JL, Rosenblum M, et al. Associations among magnetic resonance spectroscopy, apparent diffusion coefficients, and image-guided histopathology with special attention to radiation necrosis. Neurosurgery 2004;54:1111–9.

[40] Ganslandt O, Stadlbauer A, Fahlbusch R, Kamada K, Buslei R, Blumcke I, et al. Proton magnetic resonance spectroscopic imaging integrated into image-guided surgery: correlation to standard magnetic resonance imaging and tumor cell density. Neurosurgery 2005;56(Suppl. 2)):291–8.

[41] Hall WA, Truwit CL. 1.5 T: spectroscopy-supported brain biopsy. Neurosurg Clin N Am 2005;16:165–72.

[42] McKnight TR, Lamborn KR, Love TD, Berger MS, Chang S, Dillon WP, et al. Correlation of magnetic resonance spectroscopic and growth characteristics within Grades II and Grades III gliomas. J Neurosurg 2007;106:660–6.

[43] Sibtain NA, Howe FA, Saunders DE. The clinical value of proton magnetic resonance spectroscopy in adult brain tumours. Clin Radiol 2007;62:109–19.

[44] Hermann EJ, Hattingen E, Krauss JK, Marquardt G, Pilatus U, Franz K, et al. Stereotactic biopsy in gliomas guided by 3-Tesla 1H-chemical-shift imaging of choline. Stereotact Funct Neurosurg 2008;86:300–7.

[45] Ng WH, Lim T. Targeting regions with highest lipid content on MR spectroscopy may improve diagnostic yield in stereotactic biopsy. J Clin Neurosci 2008;15:502–6.

[46] Muragaki Y, Chernov M, Maruyama T, Ochiai T, Taira T, Kubo O, et al. Low-grade glioma on stereotactic biopsy: how often is the diagnosis accurate? Minim Invasive Neurosurg 2008;51:275–9.

[47] Louis DN, Ohgaki H, Wiestler OD, Cavenee WK, editors. WHO Classification of Tumours of the Central Nervous System. Lyon: IARC; 2007.

[48] Mork SJ, Halvorsen TB, Lindegaard K-F, Eide GE. Oligodendroglioma: histologic evaluation and prognosis. J Neuropathol Exp Neurol 1986;45:65–78.

[49] Muragaki Y, Iseki H, Maruyama T, Kawamata T, Yamane F, Nakamura R, et al. Usefulness of intraoperative magnetic resonance imaging for glioma surgery. Acta Neurochir Suppl 2006;98:67–75.

[50] Kelly PJ, Daumas-Duport C, Kispert DB, Kall BA, Scheithauer BW, Illig J. Imaging-based stereotaxic serial biopsies in untreated intracranial glial neoplasms. J Neurosurg 1987;66:865–74.

[51] Greene GM, Hitchon PW, Schelper RL, Yuh W, Dyste GN. Diagnostic yield in CT-guided stereotactic biopsy of gliomas. J Neurosurg 1989;71:494–7.

[52] Negendank WG, Sauter R, Brown TR, Evelhoch JL, Falini A, Gotsis ED, et al. Proton magnetic resonance spectroscopy in patients with glial tumors: a multicenter study. J Neurosurg 1996;84:449–58.

[53] Shimizu H, Kumabe T, Tominaga T, Kayama T, Hara K, Ono Y, et al. Noninvasive evaluation of malignancy of brain tumors with proton MR spectroscopy. AJNR Am J Neuroradiol 1996;17:737–47.

[54] Tedeschi G, Lundbom N, Raman R, Bonavita S, Duyn JH, Alger JR, et al. Increased choline signal coinciding with malignant degeneration of cerebral gliomas: a serial proton magnetic resonance spectroscopy imaging study. J Neurosurg 1997;87:516–24.

[55] Meyerand ME, Pipas JM, Mamourian A, Tosteson TD, Dunn JF. Classification of biopsy-confirmed brain tumors using single-voxel MR spectroscopy. AJNR Am J Neuroradiol 1999;20:117–23.

[56] Shimizu H, Kumabe T, Shirane R, Yoshimoto T. Correlation between choline level measured by proton MR spectroscopy and Ki-67 labeling index in gliomas. AJNR Am J Neuroradiol 2000;21:659–65.

[57] Tamiya T, Kinoshita K, Ono Y, Matsumoto K, Furuta T, Ohmoto T. Proton magnetic resonance spectroscopy reflects cellular proliferative activity in astrocytomas. Neuroradiology 2000;42:333–8.

[58] Moller-Hartmann W, Herminghaus S, Krings T, Marquardt G, Lanfermann H, Pilatus U, et al. Clinical application of proton magnetic resonance spectroscopy in the diagnosis of intracranial mass lesions. Neuroradiology 2002;44:371–81.

[59] Calvar JA, Meli FJ, Romero C, Calcagno ML, Yanez P, Martinez AR, et al. Characterization of brain tumors by MRS, DWI and Ki-67 labeling index. J Neurooncol 2005;72:273–80.

[60] Preul MC, Leblanc R, Caramanos Z, Kasrai R, Narayanan S, Arnold DL. Magnetic resonance spectroscopy guided brain tumor resection: differentiation between recurrent glioma and radiation change in two diagnostically difficult cases. Can J Neurol Sci 1998;25:13–22.

[61] Stadlbauer A, Moser E, Gruber S, Nimsky C, Fahlbusch R, Ganslandt O. Integration of biochemical images of a tumor into frameless stereotaxy achieved using a magnetic resonance imaging/magnetic resonance spectroscopy hybrid data set. J Neurosurg 2004;101:287–94.

[62] Dowling C, Bollen AW, Noworolski SM, McDermott MW, Barbaro NM, Day MR, et al. Preoperative proton MR spectroscopic imaging of brain tumors: correlation with histopathologic analysis of resection specimens. AJNR Am J Neuroradiol 2001;22:604–12.